Bull. Mater. Sci., Vol. 40, No. 2, April 2017, pp. 271–280. © Indian Academy of Sciences.
DOI 10.1007/s12034-017-1382-4

# Anatase–CMK-3 nanocomposite development for hydrogen uptake and storage

**MARCOS B GÓMEZ COSTA[1], JULIANA M JUÁREZ[1], GINA PECCHI[2] and OSCAR A ANUNZIATA[1,*]**

[1]Centro de Investigación en Nanociencia y Nanotecnología (NANOTEC), Facultad Regional Córdoba, Universidad Tecnológica Nacional, Maestro López y Cruz Roja Argentina, 5016 Córdoba, Argentina
[2]Departamento de Físico-Química, Facultad de Ciencias Químicas, Universidad de Concepción, Casilla 3-C, Concepción 4070386, Chile

MS received 7 October 2015; accepted 13 March 2017

**Abstract.** **The nanometric carbon CMK-3 modified with $TiO_2$ in anatase phase was synthesized and applied to energy uptake and storage. $TiO_2$ nanoclusters are important for hydrogen energy harvesting. The creation of porous structures or large surface with $TiO_2$ nanoclusters inside can potentially face the challenge of improving their efficiency. In the present work, we report the synthesis and characterization of $TiO_2$–CMK-3 material assembled from anatase nanoparticles dispersed in the nanometric carbon CMK-3. The resulting nanocomposite was characterized by X-ray diffraction, Raman spectroscopy, transmission electron microscopy, X-ray photoelectron spectroscopy, energy-dispersive X-ray spectroscopy and $N_2$ adsorption–desorption analysis. The newly synthesized hybrid composites exhibited significantly enhanced $H_2$ storage, in which CMK-3-ordered porous carbon modified with anatase nanoclusters proved to be a material for hydrogen uptake. The nanoparticles of anatase (∼5 nm) incorporated onto CMK-3 showed higher hydrogen uptake at low and high pressures (2.9 wt% of $H_2$ sorption at 10 bar and 77 K) than CMK-3. The approach includes a discussion of $H_2$ adsorption process and storage properties.**

**Keywords.** **Nanocomposite; anatase; CMK-3; hydrogen; storage.**

## 1. Introduction

Hydrogen is considered as a clean energy carrier and an alternative fuel source for many applications. Some keys to use hydrogen, as fuel, are its safe storage, low cost, lightweight, and reversible, with simple adsorption–desorption kinetics. However, a common limitation is the weak van der Waals interaction between molecular hydrogen and host material. Hence, to enhance hydrogen binding, low amounts of transition metals or cations are added to improve hydrogen sorption. Physisorption of hydrogen on carbon-based nanomaterials or other porous materials has attracted considerable scientific interest. Porous carbons with well-ordered pore systems have offered great potential in hydrogen storage [1–4].

Metal–organic frameworks (MOFs) are particulary promising candidates in the field of gas separation and storage. A large portion of voids generated in MOFs usually remains unused for hydrogen storage because of weak interactions between the walls of MOFs and $H_2$ molecules. Saha and Deng [5] synthesized mixed crystals of MOF-5 and MOF-177 in order to determine hydrogen adsorption at a hydrogen pressure up to 1.05 bar and at different temperatures (77, 194.5 and 298 K).

Many activated and templated carbons with high-surface area exhibit potential for storing molecular hydrogen [6–9]. Nanostructured carbons are among the major candidates of physisorption due to their lightweight, low cost and abundant natural precursors. The activated carbons have been reported to have relatively high hydrogen storage capacity at 77 K [7,8]; yet pore size distribution is generally wide and more than half of the total porous volume comes from macropores, which contribute less to the uptake of hydrogen.

Carbons mesostructured from Korea (CMK) comprise one such family of ordered mesoporous carbons (OMCs) [10]. Produced inside the channels of mesostructured silicates or aluminosilicates, CMK have specific surface areas from 1000 to 2000 $m^2\ g^{-1}$ and pore volumes from 0.5 to over 1 $ml\ g^{-1}$. These materials are promising for hydrogen storage applications. The carbons were obtained via the template method, which involves the introduction of appropriate carbon precursors into the ordered pores of the template followed by carbonization and removal of the template. These carbon materials usually have large surface areas and high pore volumes, which are useful for effective physisorption of $H_2$.

Thus, CMK-3 was chosen as an ideal candidate as a support material for hydrogen storage due to its large surface area, high chemical stability, uniform pore diameter, accessible porosity and three-dimensional conducting network [11,12].

*Author for correspondence (oanunziata@scdt.frc.utn.edu.ar)

Metal particles dispersed in the pores of active carbons largely contribute to enhancing storage abilities. We can find numerous studies focused on this feature, and generally, hydrogen spillover is evidenced. The catalyst is supposed to trigger the $H_2$ dissociation, and atomic hydrogen is assumed to diffuse deeper in the microporous network, and even in between graphitic layers. Xia *et al* [13] studied $CO_2$ activation effect in ordered porous carbon CMK-3 applied to hydrogen storage. The $H_2$ adsorption of CMK-1 was around 1.2 wt% at 1 bar and that of the activated CMK-3 around 2%. Kim *et al* [14] investigated OMCs as support materials for Pt catalysts for oxygen reduction reaction (ORR).

Juárez *et al* [15,16] reported Pt–CMK-3, Zn–CMK-1 and Ni–CMK-3 as promising hydrogen storage nanomaterials. The adsorption in these materials was fully reversible and higher than that in carbon hosts.

$TiO_2$ has been studied as a metal oxide in scientific and technological applications for its chemical and physical properties. Commercially, $TiO_2$ is used in many applications, such as toxic material conversion, solar cells, air purification, environmental applications, etc. [17,18].

$TiO_2$ is one of the important metal oxides for a broad range of $H_2$ gas sensing applications because of its surface chemistry and structure, charge transport and electrical properties. Anatase, rutile and brookite are natural polymorphs of $TiO_2$. The brookite phase has mechanical and thermal properties similar to those of the rutile phase. The rutile phase is a thermodynamically more stable phase than the anatase phase at high temperature. However, it has been shown that electron transport is slower in the rutile and brookite layers than in the anatase layer because of a difference in the extent of interparticle connectivity associated with particle packing density [19].

At present, nanostructured $TiO_2$ is also considered as a promising photocatalyst for hydrogen production, since it exhibits superior photocatalytic activity compared with that of traditional bulk materials [20,21]. There is a growing tendency to integrate specialized nanostructures into photocatalysts, such as mesoporous carbon materials and nanotube/nanowire arrays, in order to enhance energy collection and storage, and to address new challenges in hydrogen production or other energy applications [22–24]. CMK-3 possesses high surface area, low density, delivering ability, surface permeability and high collecting capacities, which enhance the adsorption activity of $TiO_2$. For hydrogen energy application, an important factor influencing hydrogen evolution in porous materials is the value of grain surface area; the larger the surface area, the higher amount of the hydrogen adsorption. Therefore, facile ways for the formation of $TiO_2$ nanoclusters are quite attractive.

Liu *et al* [25] reported sol–gel fabrication of mesoporous $TiO_2$ microspheres assembled from nanoparticles with the assistance of gelatin template. With gelatin assistance they fabricated 10–20 nm $TiO_2$ nanoparticles. With the increase of gelatin addition, $TiO_2$ microspheres exhibited a marked increase in $H_2$ storage capacities, especially at high pressures; with a 5% gelatin additive, the sample exhibited a much higher hydrogen uptake of 6 mol% up to 90 bar.

Chu *et al* [26] proposed a system with the potential of a good candidate for hydrogen storage, in which multiple hydrogen molecules can be adsorbed in the ground state around an impurity in graphene at a certain optimal interlayer distance (ILD). The first-principle calculations predict that this complex, Ti atom embedded in double-vacancy graphene, can hold up to eight $H_2$ per unit. Shalabi *et al* [27] reported the hydrogen storage reactions on Ti-decorated carbon nanocones by using the state-of-the-art density functional theory calculations. The single Ti atom prefers binding at the bridge site between two hexagonal rings, and can bind up to six hydrogen molecules with average adsorption.

The anatase activity in adsorption of hydrogen molecules is improved, producing significant changes in hydrogen sorption properties. After anatase–CMK-3 impregnation, a loss of specific surface area and total pore volume was observed. However, at 77 K the hydrogen uptake was found to be better than that with pristine material, which improved the hydrogen uptake, leading to enhanced adsorption mechanism and the possibility of promoting the adsorption of molecular hydrogen on the surface of anatase nanoparticles, in addition to a further hydrogen diffusion into the pores of carbon. This material improves the hydrogen uptake capacity of CMK-3 nanometric carbon.

In this work, ordered porous carbon, referred to as CMK-3, was synthesized by replication from SBA-15 silica, and afterwards modified with anatase in order to gain higher hydrogen storage capacity. $TiO_2$ in anatase phase clusters dispersed on CMK-3 support of large particle size and long channel lengths shows a design that enhances the hydrogen uptake. This research includes synthesis and characterization of carbon-modified nanostructures along with experimental study of their adsorption capacity and storage properties.

## 2. Material and methods

### 2.1 *Materials*

Tetraethylorthosilicate (TEOS, 98%, Sigma-Aldrich), poly(ethylene glycol)-block-poly(propylene glycol)-block-poly(ethylene glycol), ($EO_{20}PO_{70}EO_{20}$, P123-Sigma-Aldrich), sucrose (≥99.0%, FLUKA) and tetrabutyl orthotitanate (TBOT, >97%, Fluka).

### 2.2 *Synthesis of Si-SBA-15*

For the synthesis of CMK-3, SBA-15 was used as the template. The synthesis of ordered mesoporous silica SBA-15 was prepared according to previous work [15]. Typically 20 g of P123 (poly(ethylene glycol)-block-poly(propylene glycol)-block-poly(ethylene glycol)) was dissolved at 323 K in 1 M HCl solution. Then, 40 g of TEOS was added and the resulting mixture was stirred at 323 K for 24 h. The milky mixture was transferred into a polypropylene bottle and kept at 373 K for 72 h. The resultant solid was filtered and washed with deionized water until pH∼6. The molar composition was Si: 0.018 $EO_{20}PO_{70}EO_{20}$: 2.08 HCl: 112 $H_2O$.

In order to extract the template, the material was first immersed in ethanol reflux for 6 h. The product was filtered, washed and dried in air at 363 K [28]. To ensure elimination of the structure-directing agent, the sample was heated in $N_2$ flow, at 20 ml $min^{-1}$ and 573 K, and then calcined at 823 K in air for 6 h.

### 2.3 *Synthesis of CMK-3 carbon*

The synthesis of CMK-3 mesopourous carbon was carried out using SBA-15 as a hard template and sucrose as carbon precursor, following the synthesis procedure described by Juárez *et al* [15]. Briefly, 1.1 g of sucrose was dissolved in a solution of $H_2SO_4$ (0.14 g) in water (5 g) and to this solution, 1 g of SBA-15 was added. The resulting mixture was dried at 373 K and then heated at 433 K for 6 h. A second impregnation was performed in order to ensure the filling of the template pores with the carbon precursor, using $H_2SO_4$ solution with 0.75 g of sucrose. The mixture was dried at 373 K and heated at 433 K for 6 h. This brown powder was then heated to 1173 K in nitrogen flow (20 ml $min^{-1}$).

Silica removal was performed using HF solution (5 wt%) at room temperature. The carbon sample was filtered, washed with ethanol solution and dried at 393 K.

### 2.4 *Synthesis of $TiO_2$–CMK-3*

$TiO_2$ nanoparticles were incorporated into OMC CMK-3 using wet impregnation and TBOT as a Ti source. The metal precursor (TBOT) was dissolved in 10 ml of ethanol by vigorous stirring, to reach a nominal content of 5 wt% of Ti in the final solid. CMK-3 was incorporated in the solution and both were placed in a rotary evaporator to remove excess of ethanol at 313 K and 60 rpm. The powder was then dried at 373 K overnight. Finally, the resulting material was heated in a dynamic inert atmosphere ($N_2$ flow of 20 ml $min^{-1}$) from 298 to 473 K with a slope of 4 K $min^{-1}$; temperature was then increased to 743 K with a slope of 10 K $min^{-1}$ and kept at this temperature for 5 h.

### 2.5 *Characterization*

The X-ray diffraction (XRD) patterns were recorded with an X'Pert Pro PANalytical diffractometer equipped with a CuK$\alpha$ radiation source (K$\alpha = 0.15418$ nm) and an X'Celerator detector based on real-time multiple strips (RTMS). The samples were ground and placed on a stainless-steel plate. Diffractograms were analysed with X'PertHighScore Plus software and JCPDS-ICDD data library. Nitrogen adsorption–desorption isotherms at 77 K were measured on an ASAP 2020 equipment after degassing the samples at 673 K, to determine textural properties such as surface area and pore volume; pore size distribution was estimated using the Barrett, Joyner and Halenda (BJH) algorithm. Transmission electron microscopy (TEM) micrographs were obtained on a JEOL model JEM-1200 EX II microscope; samples were prepared by drying the dispersion on amorphous carbon-coated copper grids. Raman spectrum was obtained using an InVia Reflex Raman microscope and spectrometer and 532 nm diode laser excitation. X-ray photoelectron spectra (XPS) were obtained on a MicrotechMultilb 3000 spectrometer, equipped with a hemispherical electron analyser and MgK$\alpha$ ($h\nu = 1253.6$ eV) photon source. An estimated error of $\pm 0.1$ eV can be assumed for all measurements. Peak intensity was calculated from the respective peak areas after background subtraction and spectrum fitting by a combination of Gaussian/Lorentzian functions. Energy-dispersive X-ray (EDX) analyses were coupled to the scanning electron microscopy (SEM, LEO Mod. 440 equipment). Hydrogen storage isotherms at low and high pressure (up to 10 bar) and 77 K were measured using an ASAP 2050 equipment appropriately calibrated. Before hydrogen storage test, metal-doped carbons were heated in high vacuum at a milder temperature of 523 K, for at least 8 h, avoiding the possible decomposition of the metal nanoparticles at a higher temperature treatment. They were then cooled to room temperature. For the adsorption experiments, high-purity hydrogen gas (99.9999%) was used in the equipment. For the samples, hydrogen storage capacity was measured in a pressure range from 0 to 10 bar.

## 3. Results and discussion

### 3.1 *XRD analysis*

Low-angle XRD patterns for SBA-15, CMK-3 and $TiO_2$–CMK-3 are shown in figure 1. The hard template SBA-15 shows excellent structural order for the hexagonal P6mm crystallographic space group. The mesoporous carbon CMK-3 pattern, obtained by hard templating of SBA-15, indicates that the carbon CMK-3 is an exact replica of the template, demonstrated by the appearance of peaks consistent with the symmetry of SBA-15 [29].

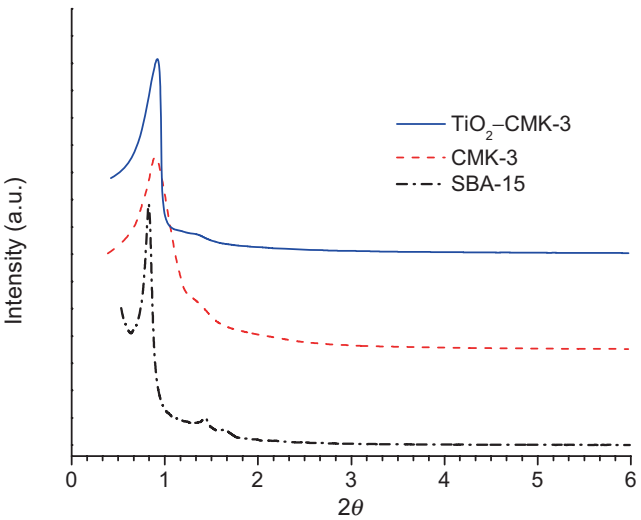


**Figure 1.** Small-angle XRD patterns of SBA-15, CMK-3 and $TiO_2$–CMK-3.

**Table 1.** XRD parameters of samples.

| | SBA-15 [*h k l*] | | | CMK-3 [*h k l*] | | | |
|---|---|---|---|---|---|---|---|
| | [1 0 0] | [1 1 0] | [2 0 0] | [1 0 0] | [1 1 0] | [2 0 0] | |
| Sample | *d* (nm) | | | *d* (nm) | | | $a_0$ (nm) |
| SBA-15 | 8.6 | 5.0 | 4.3 | — | — | — | 10.0 |
| CMK-3 | — | — | — | 10.5 | 6.1 | 5.2 | 12.1 |
| $TiO_2$–CMK-3 | — | — | — | 8.3 | 8.8 | 8.7 | 8.6 |

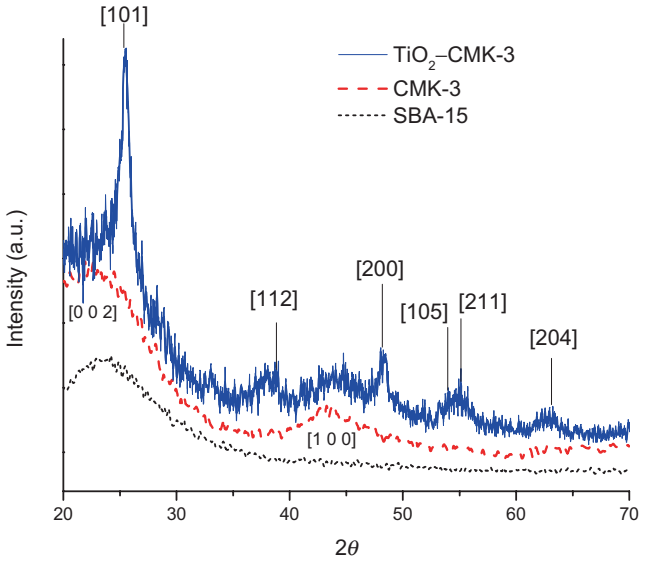


**Figure 2.** Wide-angle XRD patterns of SBA-15, CMK-3 and $TiO_2$–CMK-3.

When $TiO_2$ was incorporated to the carbon structure, the overall pore framework was maintained as indicated by the presence of low-angle diffraction peaks (see table 1).

Figure 2 shows the wide-angle X-ray diffraction patterns for CMK-3 and $TiO_2$–CMK-3. In both cases, two broad diffraction peaks are distinguished, which can be indexed as [0 0 2] and [1 0 0] diffraction for typical graphite carbons [30].

The pattern of $TiO_2$–CMK-3 shows characteristic signals of $TiO_2$ in anatase phase [31], indicating a particularly good synthesis process. The absence of prominent reflections in $TiO_2$ clusters indicates that no crystalline bulk material has been formed [32], with nanometric size and high dispersion (very broad XRD $TiO_2$ signals, figure 2). This can be ascribed to a relatively low scattering contrast between the pores and walls of mesoporous materials, due to the formation of anatase nanoclusters, which depict fine dispersion on CMK-3 with a narrow size distribution [33].

While the nanomaterial area is smaller with the incorporation of $TiO_2$, the characteristic structure of CMK-3 is maintained after the metal is within the host, in agreement with XRD studies.

The XRD patterns analysis allows determining the crystals size of anatase particles in the samples, and the effect obtained on metal dispersion. The average cluster size was

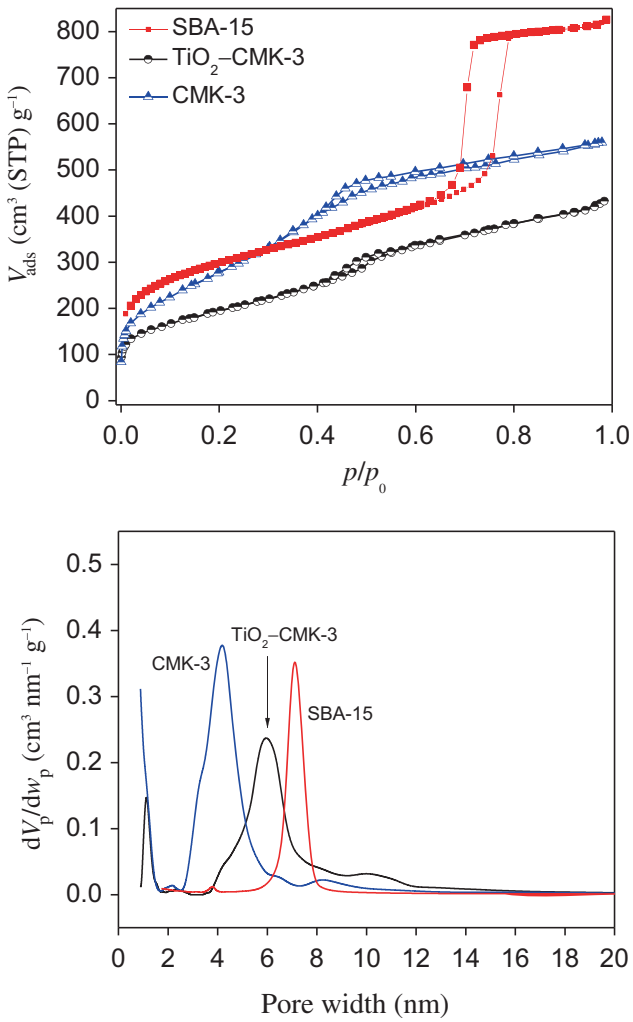


**Figure 3.** Nitrogen adsorption (solid lines)–desorption isotherm (symbols) at 77 K and pore size distribution of (a) SBA-15, (b) CMK-3 and (c) $TiO_2$–CMK-3.

estimated from the width of the diffraction peaks corresponding to different [*h k l*] Miller indices using Scherrer's formula [34]. The average diameter of anatase particles obtained by Scherrer's formula was ~5 nm.

### 3.2 *Adsorption–desorption isotherms analysis*

Figure 3 shows the $N_2$ adsorption–desorption isotherms for SBA-15, CMK-3 and $TiO_2$–CMK-3 samples at 77 K; table 2

**Table 2.** Textural properties of the materials and composite.

| Material | $S_{BET}$ ($m^2\ g^{-1}$) | $V_{\mu P}$ ($cm^3\ g^{-1}$) | $V_{TP}$ ($cm^3\ g^{-1}$) | $W_p$ (nm) |
|---|---|---|---|---|
| $TiO_2$–CMK-3 | 706 | 0.11 | 0.67 | 6 |
| CMK-3 | 1323 | 0.23 | 1.01 | 4.5 |
| SBA-15 | 1040 | 0.57 | 1.38 | 7 |

$V_{TP}$: total pore volume; $S_{BET}$: BET surface area; $V_{\mu P}$: micropore volume; $W_P$: wide mesopore.

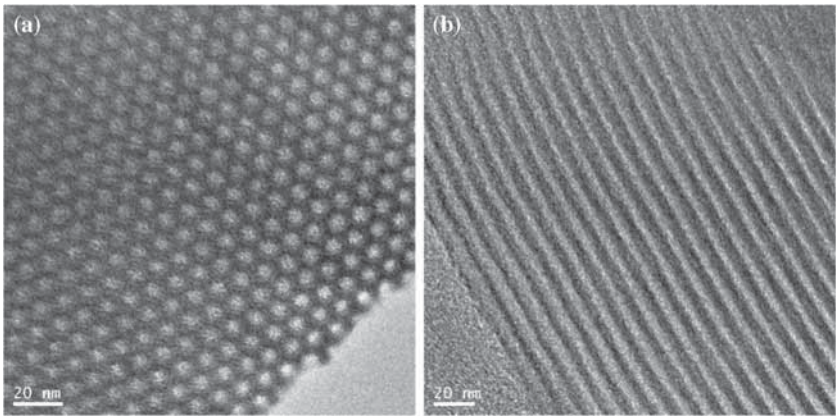


**Figure 4.** TEM images of SBA-15: (**a**) [1 0 0] and (**b**) [1 1 0] reflection planes.

displays the textural properties determined from nitrogen physisorption analysis. The isotherm for SBA-15 is a typical type IV curve with hysteresis loop, according to IUPAC classification, revealing the mesoporous nature of the material.

The nitrogen adsorption–desorption isotherms for CMK-3 and $TiO_2$–CMK-3 are typical type IV curves exhibiting hysteresis loops of type $H_2$, according to IUPAC classification, typical of mesoporous solids.

The materials obtained exhibit capillary condensation to relative pressures of about 0.40 and 0.45, which can be related to the pore-blocking effect of influencing pressure where evaporation/desorption pore occurs. The increase in adsorption at low relative pressures is associated with the presence of micropores or a strong adsorbate–adsorbent interaction.

$TiO_2$–CMK-3 reveals a reduced specific surface area, in comparison with those of pure SBA-15 and CMK-3, with incorporated anatase nanoparticles.

The pore size distribution of CMK-3 shows a sharp peak at 4.2 nm, which indicates a quite regular array of nanopores. In contrast, pore size distribution of $TiO_2$–CMK-3 shows a broad peak with a maximum at approximately 6 nm, which corresponds to primary mesopores.

### 3.3 *XPS and EDX characterization*

As estimated by XPS analysis of $TiO_2$–CMK-3 (the spectra not shown), Ti signal appears at 458.5 eV (Ti $2p_{3/2}$), indicating that Ti is incorporated in the mesoporous nanostructure of CMK-3, as anatase phase [35,36]. The spectra for C 1s peak for CMK-3 show a main peak at 284.5 eV attributed to disordered graphitic structure species as well as C $sp^2$ and C $sp^3$ bonding [37]. According to XPS results, the atomic ratio of C–Ti (560) for $TiO_2$–CMK-3 indicates that Ti species are well dispersed in the mesopores of CMK-3 due to the low signal observed in XPS analysis (50–100 Å of depth), most of which is within the pore nanostructure. On the other hand, this is confirmed by the results obtained by EDX for C–Ti ratio (78), higher than that obtained by XPS.

### 3.4 *TEM studies*

TEM images (figure 4) show typical framework of SBA-15 inorganic template with a regular array of nanometric longitudinal channels of 7 nm diameter separated by inorganic Si–O walls. Figure 5a shows TEM images of CMK-3. The image reveals particles of the nanometric carbon consisting of many rope-like domains (rod-like particles) with relatively uniform sizes of about 1 μm length and 0.2 μm width. Figure 5b and c shows that the CMK-3 sample consists of uniform carbon rods and high pore volume resulting from mesopores between carbon rods. Some irregularities in the channels were attributed to an incomplete filling of SBA-15 meso-tunnels with carbon precursor, due to the presence of a fraction of nonlinear channels in SBA-15.

TEM images for $TiO_2$–CMK-3 (figure 6) show an ordered structure slightly damaged by thermal treatments; they also exhibit well-organized pores parallel to each other. The white lines correspond to the mesopores generated in the space previously occupied by the walls of SBA-15 template.

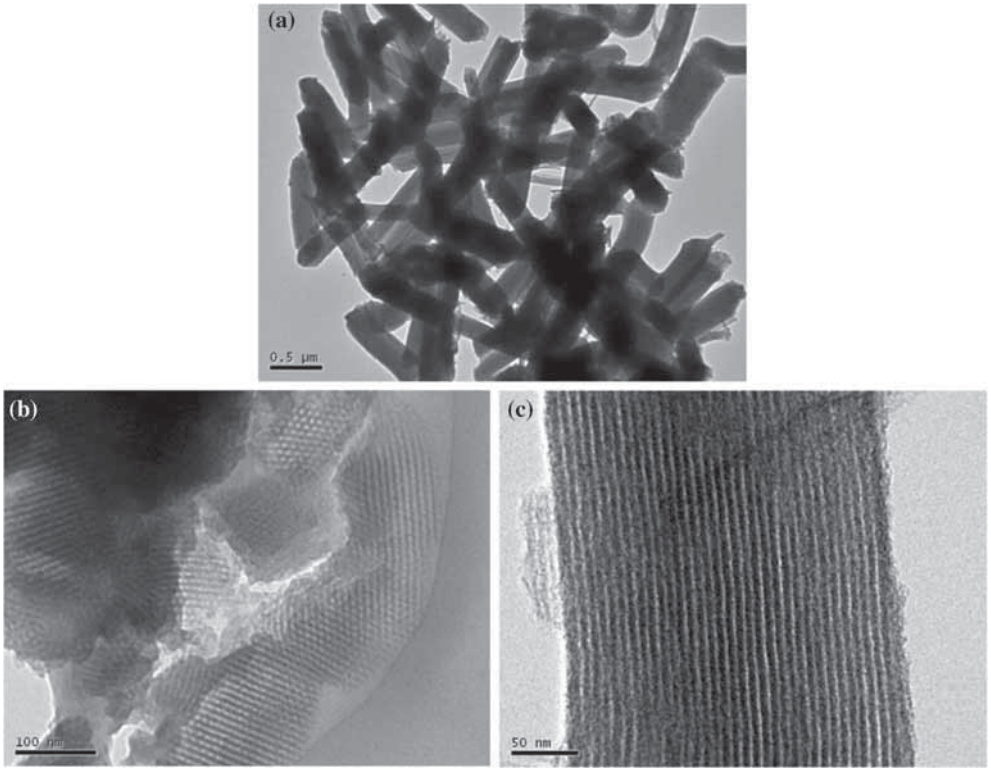


**Figure 5.** TEM images of CMK-3: (**a**) nanoparticles, (**b**) [1 0 0] and (**c**) [1 1 0] reflection planes.

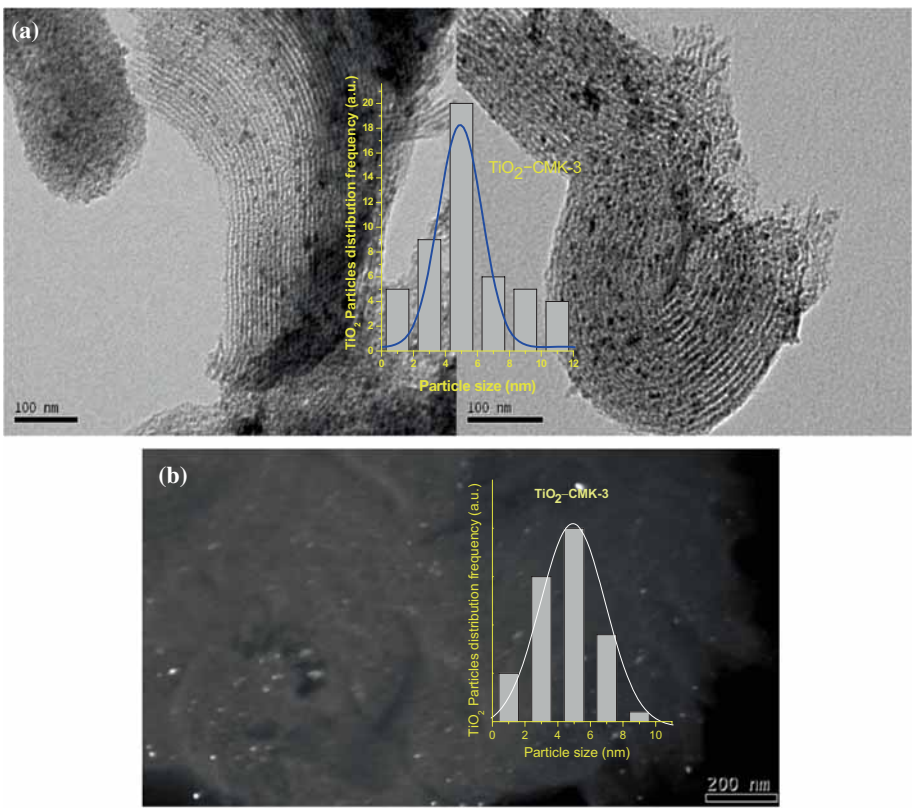


**Figure 6.** (**a**) TEM images and particle size distribution histogram of $TiO_2$–CMK-3. (**b**) Negative contrast image.

In figure 6, the dark spot indicates anatase nanoclusters. Figure 6b shows a TEM image with negative contrast, displaying nanoclusters with bright spots, allowing the observation of nanoclusters. Particle size distribution ranged from 1 to 11 nm and mean particle diameter was found to be close to 5 nm, indicating that most of the particles reside within the pore system. In this work, we show that the nature of $TiO_2$ incorporation into CMK-3 and the preparation of $TiO_2$–CMK-3 (in $N_2$ atmosphere and controlled temperature elimination of Ti precursor) influence posterior $TiO_2$ nanoparticle size, leading to a narrow distribution as shown in the histograms (figure 6).

### 3.5 *Raman studies*

Figure 7 shows Raman spectra of SBA-15, pristine host CMK-3, $TiO_2$–CMK-3 and pure anatase and rutile in the range of 200–1200 $cm^{-1}$.

For SBA-15, Raman bands at 430, 800 and 1080 $cm^{-1}$ are observed. The bands at 430 and 1080 $cm^{-1}$ can be attributed to symmetric and asymmetric vibrations of the Si–O–Si unit, respectively. The band at 800 $cm^{-1}$ is the symmetric stretching mode of the tetrahedral [$SiO_4$] unit [38–40]. Figure 7 also shows the spectra of $TiO_2$ onto CMK-3; the characteristic signals of anatase are detected in the sample if compared with those of pure anatase [39] and pure rutile.

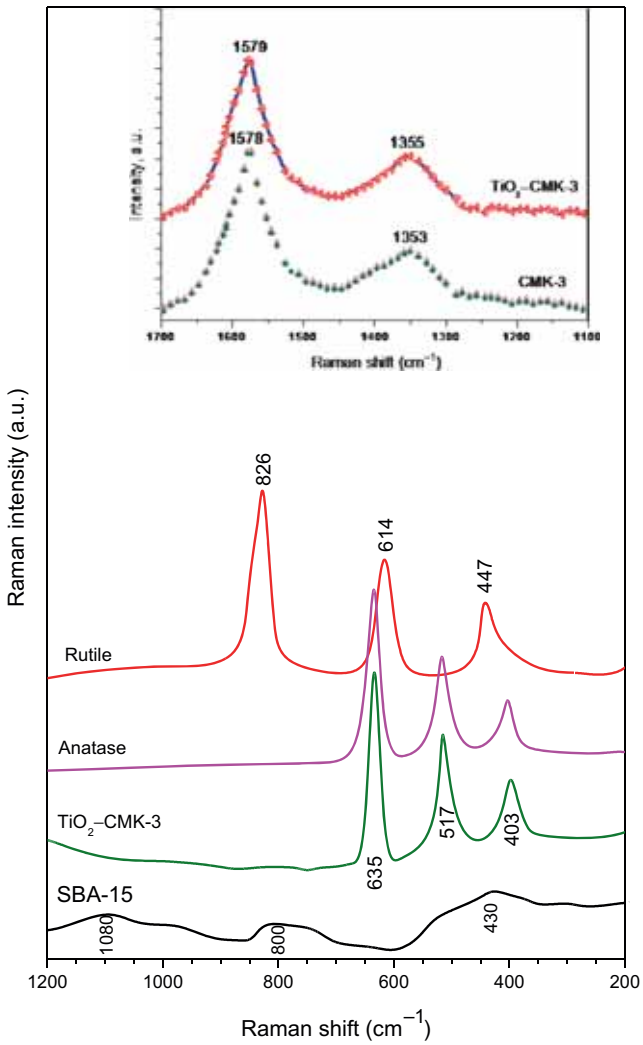


**Figure 7.** Raman spectra of SBA-15, $TiO_2$–CMK-3, rutile, anatase and CMK-3 (inset).

In the inset of figure 7, we illustrate the Raman spectra of bare CMK-3 and $TiO_2$–CMK-3 (from 1100 to 1700 $cm^{-1}$). The Raman spectrum of the obtained CMK-3 as well as $TiO_2$–CMK-3 shows two peaks, at 1578 and 1353 $cm^{-1}$. The peak at 1578 $cm^{-1}$ corresponds to an $E_{2g}$ mode of graphite, and is called G band, related to C=C double bonded carbon vibration in hexagonal lattice, while the peak at 1353 $cm^{-1}$ is associated with vibrations of C–C bond, referred to as D band, attributed to the configuration of disordered graphite [41–43]. In the Raman spectrum of graphitic materials like activated charcoal, carbon black and CMK this second line appears. The relative intensity of the two lines depends on the type of graphitic material. The intensity of 1353 $cm^{-1}$ line increases with an increase in carbon in the samples and with a decrease in the graphite crystal size. Hence, a signal at 1355 $cm^{-1}$ might possibly be ascribed to a diamond-like atomic arrangement in the graphite samples, probably as partially tetrahedrally bonded [44]. This is in agreement with the suggestion of Darmstadt *et al* [45], who proposed a graphite-like structure for CMK-3. It could be clearly seen that G and D band intensity of $TiO_2$–CMK-3 was not perturbed significantly (inset of figure 7).

### 3.6 *Hydrogen uptake measurements*

The capacity of hydrogen storage was evaluated at low and high pressures and cryogenic temperatures (77 K). The experimental data were fitted by the Freundlich isotherm equation, a purely empirical formula for gaseous adsorbates. The Freundlich model has been described by Juárez *et al* [15,16]. For this fit, least-square nonlinear regression was used for arbitrary fit functions and for minimizing the objective function by the Levenberg–Marquardt method. The fitting accuracy was $R^2 = 0.98$.

Figure 8 shows the adsorption–desorption isotherms of hydrogen at 77 K on CMK-3 and $TiO_2$–CMK-3 samples at a range of pressures (0–10 bar). The inset of this figure shows behaviour at low pressures (0–1 bar). As we can see in this figure, anatase–CMK-3 and CMK-3 carbon are not comparable materials in hydrogen storage. Anatase–CMK-3 has $TiO_2$ nanoclusters as anatase phase dispersed in CMK-3 framework, which increase the hydrogen storage in CMK-3 carbon.

At low and high pressures, the amount of hydrogen uptake is higher in $TiO_2$–CMK-3 sample than in CMK-3 sample. We employed the term 'uptake' as storage (carbon like a sponge), because the process of hydrogen adsorption was completely reversible [46], indicating absence of chemical reaction or strong bond between hydrogen and $TiO_2$ nanocluster or CMK-3 framework (curves coincide, since every point returns to the initial value).

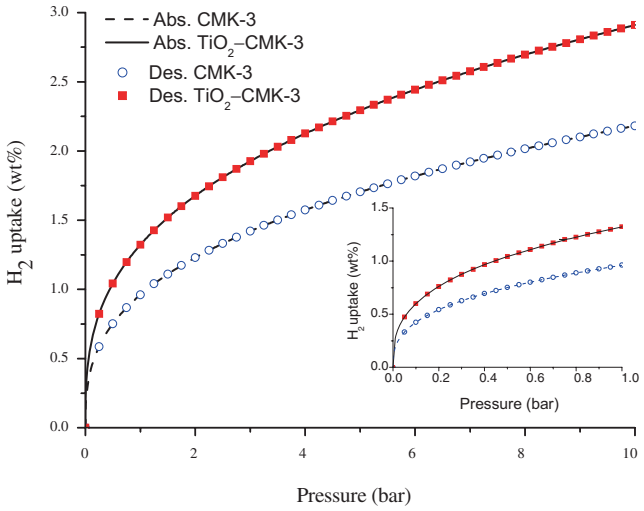


**Figure 8.** $H_2$ adsorption–desorption isotherms of CMK-3 and $TiO_2$–CMK-3.

There are two different processes involved in the hydrogen adsorption on the $TiO_2$–CMK-3 surface: hydrogen molecules can spill over onto CMK-3 nano/micropores and get adsorbed on nanometric anatase clusters.

First, we could attribute this adsorption to the different particle surface areas, since the adsorbed quantity might be primarily related to the available free surface area. Second, we could attribute it to the fact that nanometric carbon supports the high surface areas of $TiO_2$ nanoclusters. This may possibly lead to modification of oxidation state and control of porosity feature, which is important to cause hydrogen adsorption ($H_2$ molecules) by weak chemical pathways (such as dihydrogen complex interaction), although anatase or rutile is generally weak in hydrogen storage [47]. Through XRD and TEM observation, we also noticed that with the assistance of CMK-3, the fabricated $TiO_2$ nanoparticles show small size and high dispersion, contributing to the substantial increase in $H_2$ adsorption. In other words, the presence of anatase nanoclusters in CMK-3 results in formation of better localized states of electrons at anatase nanoclusters than rutile. These localized states may distribute electron concentration at the surface of $TiO_2$–CMK-3 composite and cause weak bonds between hydrogen molecules and surface $TiO_2$ nanoclusters [47].

Anatase has a band gap greater than that of rutile. As the energy band gap is different, the Ti–Ti distances in anatase clusters are larger than in rutile. This change affects the mass density and results in a different electronic configuration. Rutile phase presents more pronounced localization of 3d states and therefore narrower 3d bands. This increases the 'power' of the electron oxidation and facilitates the transfer of electrons from $TiO_2$ to the adsorbed molecules. This explanation has also been extended to explain the activities that depend on surface orientation by suggesting that different areas have different band intervals [48]. Moreover, anatase exhibits an indirect band gap and this is smaller than its direct band gap. In rutile the fundamental band gap is also direct, or indirect band gap is very similar to direct band gap. Semiconductors that have indirect band gap generally exhibit longer lifetimes of charge carriers compared with direct gap materials. A longer life of electron–hole pair in anatase than in rutile would make it more probable to involve in surface reactions of the charge carriers [48].

According to theoretical investigations of Shalabi *et al* [27], the adsorption of the first $H_2$ molecule is therefore dissociative, with Ti–H bond. The adsorption of the first $H_2$ molecule does not affect the distance between Ti and the nearest C and consequently does not affect the interaction strength between $TiO_2$ and CMK-3. The mixed $sp^2d$ hybridization of Ti–C bonds seems to have strong repulsive effects on the adsorbed $H_2$, leading to elongation of H–H distance. Hydrogen atoms of the adsorbed $H_2$ molecule should have negative charges; $H_2$ molecule can be considered as trapped by Ti cation via the charge polarization mechanism. This indicates that Ti donates electrons to neighbouring C atoms on CMK-3, where the d-orbitals of Ti atom overlap with the $sp_2$ orbitals of Ti–C bonds to form the mixed $sp^2d$ hybridization. This charge transfer behaviour is possible since Ti atom is in cationic form and renders extensive hetero-polar bonding between the Ti atom and the nearest C atoms, resulting in an increase in $H_2$ molecule uptake. Moreover, CMK-3 approaching the positively charged Ti cation leads to loss of d-orbital degeneracy as the electrons of CMK-3 will be closer to some d-orbitals while farther away from others. Thus, d-orbitals closer to CMK-3 have a higher energy than those farther away. This results in d-orbital splitting in energy to reduce total energy and stabilize the system as explained by the ligand field theory [49].

Therefore, the first layer of hydrogen molecules could react with the metal cluster due to high oxidation/reduction metals, interacting like a dihydrogen complex [50]; yet, the amount of this initial interaction is negligible. The second layer of hydrogen molecules is physically adsorbed by dipole-induced interaction. Hydrogen molecules are non-polar; however, the strong interaction of anatase particles leads to dipole-induced effects in hydrogen molecules. The third layer and any upper layer of hydrogen molecules could interact with metal cluster by the same mechanism; however the force of dipole-induced bond is weak and decreases when distance to the surface increases. This mechanism can be applied at high pressure; consequently $TiO_2$–CMK-3 adsorbs a higher amount of hydrogen than carbon at high pressures.

The understanding of the distribution of frontier molecular orbitals around a nanostructure would be a significant guideline to design new functionalized materials for hydrogen storage. While strong localization of the highest occupied molecular orbital (HOMO) occurs on Ti cation located at the surface on anatase nanocluster, strong delocalization of the lowest unoccupied molecular orbital (LUMO) occurs at the base area. The strong localization of HOMO on Ti cation at the surface explains the enhanced adsorption interactions of $H_2$ molecule [27]. Moreover, hydrogen bonds to anatase result in an opening of HOMO–LUMO energy gap. A reduction in HOMO–LUMO energy gap for $TiO_2$–CMK-3 results

in the appearance of molecular electronic states that allow a better $H_2$ physisorption [51].

## 4. Conclusion

We have shown that a hopeful hydrogen storage material can be obtained by ordered porous carbon CMK-3 modified with $TiO_2$ species in anatase phase, synthesized by replication using SBA-15 as a template. Incorporation of anatase was carried out by wet impregnation, supported using XRD, Raman spectroscopy and adsorption–desorption $N_2$ isotherms. CMK-3 modified with anatase shows a better capacity for hydrogen uptake than that of the nanometric carbon CMK-3. The high-pressure hydrogen adsorption evolution measured at 77 K shows that $TiO_2$–CMK-3 can significantly enhance hydrogen adsorption capacity and hydrogen storage performance of CMK-3 material, proving to be prospective candidates for application in hydrogen storage.

The improved activity and the larger performance of $TiO_2$–CMK-3 is attributed to the improved dispersion of uniform anatase nanoparticles as well as to efficient use of the support, which may probably originate a high surface area and pore volume, allowing a large dispersion of anatase. Anatase nanoparticles in $TiO_2$–CMK-3 have a small size (∼5 nm average, obtained by XRD and TEM) and a quite good dispersion. Moreover, anatase nanoclusters are within the nanopores of CMK-3, according to XPS, EDS and TEM analysis.

This indicates a better hydrogen adsorption of the anatase–CMK-3 sample compared with that of CMK-3 carbon. A hydrogen storage mechanism on $TiO_2$–carbon surfaces was proposed. The mechanism of this adsorption is still under further research and optimization.

Hydrogen storage behaviours onto $TiO_2$–CMK-3 can be optimized by controlling metal cluster size and dispersion and by increasing carbon-specific surface area.

## Acknowledgement

We thank CONICET, Argentina (PIP CONICET 112201201 00218CO, 2014–2016).

## References

[1] Gadiou R, Saadallah S E, Piquero T, David P, Parmentier J and Guterl C V 2005 *Micropor. Mesopor. Mater.* **79** 121

[2] Fang B Z, Zhou H S and Honma I 2006 *J. Phys. Chem. B* **110** 4875

[3] Guterl C V, Frackowiak E, Jurewicz K, Friebe M, Parmentier J and Béguin F 2005 *Carbon* **43** 1293

[4] Yang Z X, Xia Y D, Sun X Z and Mokaya R 2006 *J. Phys. Chem. B* **110** 18424

[5] Saha D and Deng S 2009 *Int. J. Hydrogen Energy* **34** 2670

[6] Schlapbach L and Züttel A 2001 *Nature* **414** 353

[7] Kajiura H, Tsutsui S, Kadono K, Kakuta M, Ata M and Murakami Y 2003 *Appl. Phys. Lett.* **82** 1105

[8] Mandoki N T, Dentzer J, Piquero T, Saadallah S, David P and Guterl C V 2004 *Carbon* **42** 2744

[9] Züttel A, Sudan P, Mauron P, Kiyobayashi T, Emmenegger C and Schlapbach L 2002 *Int. J. Hydrogen Energy* **27** 203

[10] Yang H and Zhao D 2005 *J. Mater. Chem.* **15** 1217

[11] Anbia M and Ghaffari A 2009 *Appl. Surf. Sci.* **255** 9487

[12] Anbia M and Parvin Z 2011 *Chem. Eng. Res. Des.* **89** 641

[13] Xia K, Gao Q, Wu C, Song S and Ruan M 2007 *Carbon* **45** 1989

[14] Kim N, Yeong Cheon J, Hyung Kim J, Seong J, Park J, Joo S and Kwon K 2014 *Carbon* **72** 354

[15] Juárez J M, Gómez Costa M B and Anunziata O A 2015 *Int. J. Energy Res.* **39** 128

[16] Juárez J M, Gómez Costa M B and Anunziata O A 2015 *Int. J. Energy Res.* **39** 941

[17] Fujishima A, Rao T N and Tryk D A 2000 *J. Photochem. Photobiol. C* **1** 1

[18] Fujishima A and Zhang X T 2006 *C. R. Chim.* **9** 750

[19] Nasirian S and Milani Moghaddam H 2014 *Int. J. Hydrogen Energy* **39** 630

[20] Paronyan T M, Kechiantz A M and Lin M C 2008 *Nanotechnology* **19** 1

[21] Lin H, Huang C P, Li W, Ni C, Shah S I and Tseng Y H 2006 *Appl. Catal. B* **68** 1

[22] Ji B J, Lee I and Dahl M 2013 *Adv. Funct. Mater.* **23** 4246

[23] Edward C J W, Nakita N, Sivaram V, Tomas L, Alexander J and Snaith H J 2013 *Nature* **495** 215

[24] Renuka N K, Praveen A K and Aravindakshan K K 2013 *Mater. Lett.* **91** 118

[25] Liu B, Xiao J, Xu L, Yao Y, Costa B F O, Domingos V F, Ribeiro E S, Shi F-N, Zhou K, Su J, Wu H, Zhong K, Paixâo J A and Gil J M 2015 *Int. J. Hydrogen Energy* **40** 4945

[26] Chu S, Hu L, Hu X, Yang M and Deng J 2011 *Int. J. Hydrogen Energy* **36** 12324

[27] Shalabi A S, Taha H O, Soliman K A and Abeld S 2014 *J. Power Sources* **271** 32

[28] Meynen V, Cool P and Vansant E F 2009 *Micropor. Mesopor. Mater.* **125** 170

[29] Yang H and Zhao D 2005 *J. Mater. Chem.* **15** 1217

[30] Suryavanshi U, Iijima T, Hayashia A, Hayashi Y and Tanemura M 2012 *Chem. Eng. J.* **179** 388

[31] Khitrova V I, Bundule M F and Pinsker Z G 1977 *Kristallografiya* **22** 1253 (Calculated from ICSD using POWD-12++ 1997)

[32] Gómez Costa M B, Juárez J M, Martínez M L, Beltramone A R, Cussa J and Anunziata O A 2013 *Mater. Res. Bull.* **48** 661

[33] Veena Gopalan E, Malini K A, Santhoshkumar G, Narayanan T N, Joy P A, Al-Omari I A, Sakthi Kumar D, Yoshida Y and Anantharaman M R 2010 *Nanoscale Res. Lett.* **5** 889

[34] Langford J I and Wilson A J C 1978 *J. Appl. Crystallogr.* **11** 102

[35] Dutoit D C M, Schneider M, Hutter R and Baiker A 1996 *J. Catal.* **161** 651

[36] Atuchin V V, Kesler V G, Pervukhina N V and Zhang Z 2006 *J. Electron. Spectrosc. Relat. Phenom.* **152** 18

[37] Lezanska M, Pietrzyk O and Sojka Z 2010 *J. Phys. Chem. C* **114** 1208

[38] Bassi A L, Cattaneo D, Russo V, Bottani C E, Barborini E, Mazza T, Piseri P, Milani P, Ernst F O, Wegner K and Pratsinis S E J 2005 *J. Appl. Phys.* **98** 74305

[39] Balaji S, Djaoued Y and Robichaud J 2006 *J. Raman Spectrosc.* **37** 1416

[40] Mazza T, Barborini E, Piseri P, Milani P, Cattaneo D, Bassi A L, Bottani C E and Ducati C 2007 *Phys. Rev. B: Condens. Matter* **75** 045416

[41] Dresselhaus M S, Jorio A, Hofmann M, Dresselhaus G and Saito R 2010 *Nano Lett.* **10** 751

[42] Lu J, Yang J, Wang J, Lim A, Wang S and Loh K P 2009 *ACS Nano* **3** 2367

[43] Zhang W, Cui J, Tao C, Wu Y, Li Z, Ma L, Wen Y and Li G 2009 *Angew. Chem.* **121** 5978

[44] Tuinstra F and Koenig J L 1970 *J. Chem. Phys.* **53** 1126

[45] Darmstadt H, Roy C, Kaliaguine S, Choi S J and Ryoo R 2002 *Carbon* **40** 2673

[46] Kim B-J and Park S-J 2011 *Int. J. Hydrogen Energy* **36** 648

[47] Hoang Tuan K A and Antonelli David M 2009 *Adv. Mater.* **21** 1787

[48] Luttrell T, Halpegamage S, Tao J, Kramer A, Sutter E and Batzill M 2014 *Sci. Rep.* **4** 4043

[49] Zhang L P, Wu P and Sullivan M B 2011 *J. Phys. Chem. B* **115** 4289

[50] Takasu Y, Unwin R, Tesche B, Bradshaw A M and Grunze M 1978 *Surf. Sci.* **77** 219

[51] Nguyen T Q, Bustria Padama A A, Sison Escano M C and Kasai H 2013 *ECS Trans.* **45** 91